Computationally Intelligent Array Feed Tracking Algorithms for Large DSN Antennas

R. Mukai,[1] V. Vilnrotter,[1] P. Arabshahi,[1] and V. Jamnejad[2]

This article describes computationally intelligent neural-network and least-squares tracking algorithms for fine pointing NASA's 70-m Deep Space Network (DSN) antennas using the seven-channel Ka-band (32-GHz) array feed compensation system (AFCS). These algorithms process normalized inputs from the seven horns of the array in parallel and, hence, are less sensitive to variations in signal power and require much less time per pointing estimate than do conventional serial processing techniques (CONSCAN) currently employed by the DSN. An additional advantage of the parallel measurement technique described here is that mechanical scanning of the antenna is not required. It is shown that under nominal conditions a radial basis function (RBF) neural network trained with data from the seven array feed channels can point the antenna with less than 0.3-mdeg rms error, achieving significantly better pointing accuracy than the 0.8-mdeg requirement often quoted as a benchmark (corresponding to 0.1-dB signal-to-noise ratio (SNR) loss on 70-m antennas). Both neural-network and least-squares algorithms were simulated and compared using computer-generated antenna distortions. The results indicate that in acquisition mode the RBF neural network performs best at high SNRs; however, for low SNR applications, the least-squares algorithms yield better performance. All algorithms were shown to be strong candidates for providing excellent acquisition and tracking capabilities for the DSN's 70-m antennas.

I. Introduction

A. Tracking in the Presence of Antenna Distortions

There is increasing interest in the use of shorter carrier wavelengths to enhance the telecommunications and radio science capabilities of NASA's Deep Space Network (DSN). Shorter carrier wavelengths, or equivalently higher carrier frequencies, yield greater antenna gains and increased useful bandwidth, with reduced sensitivity to deep-space plasma effects that tend to degrade the quality of the received signal. However, there are also new problems associated with the use of higher carrier frequencies, namely greater losses due to gravity-induced deformations and wind, greater sensitivity to misalignments of the RF components, and more stringent pointing requirements further complicated by the time-varying distortions imposed on the antenna structure.

---

[1] Communications Systems and Research Section.

[2] Communications Ground Systems Section.

The research described in this publication was carried out by the Jet Propulsion Laboratory, California Institute of Technology, under a contract with the National Aeronautics and Space Administration.

As the antenna tracks the target source (whether it is a spacecraft or a radio source), time- and elevation-dependent loss components are introduced due to the Earth's rotation and the relative motion of the spacecraft, even in the absence of external disturbances. The combination of these factors can lead to unacceptably large pointing errors and signal-to-noise ratio (SNR) losses if left uncorrected. Fortunately, most of these losses can be recovered by means of a properly designed compensation and tracking system that extracts the relevant deformation and pointing information from the received signal in real time.

An accepted technique for recovering losses due to gravitational deformations, thermal distortion, and wind is by means of a real-time compensation system employing an array of feeds in the focal plane. A seven-element focal-plane array feed compensation system designed to recover gravitational losses on large DSN antennas has been constructed at the Jet Propulsion Laboratory (JPL) and evaluated at the Goldstone Deep Space Communications Complex (GDSCC). This system, called the array feed compensation system (AFCS), was developed to demonstrate real-time gravity compensation and closed-loop tracking of spacecraft and radio-source signals at Ka-band frequencies (nominally 32 GHz).

A conceptual block diagram of the Ka-band AFCS designed for the DSN's 70-m antennas is shown in Fig. 1. Its main components are an array of seven 22-dBi horns with a separate Ka-band low-noise amplifier (LNA) connected to each horn; a seven-channel downconverter assembly that converts the 32-GHz RF signal to 300-MHz IF, followed by a seven-channel baseband downconverter assembly that generates 14 real (7 complex) baseband signals; and a bank of 14 analog-to-digital converters, followed by a digital signal-processing assembly that extracts parameters from the digital samples in real time to obtain the optimum combining weights and determine the antenna-pointing updates needed to maximize the combined SNR.

In the absence of antenna distortions, a single properly designed receiving horn collects virtually all of the focused signal power. Distortions generally lead to a shift in the peak of the signal distribution as

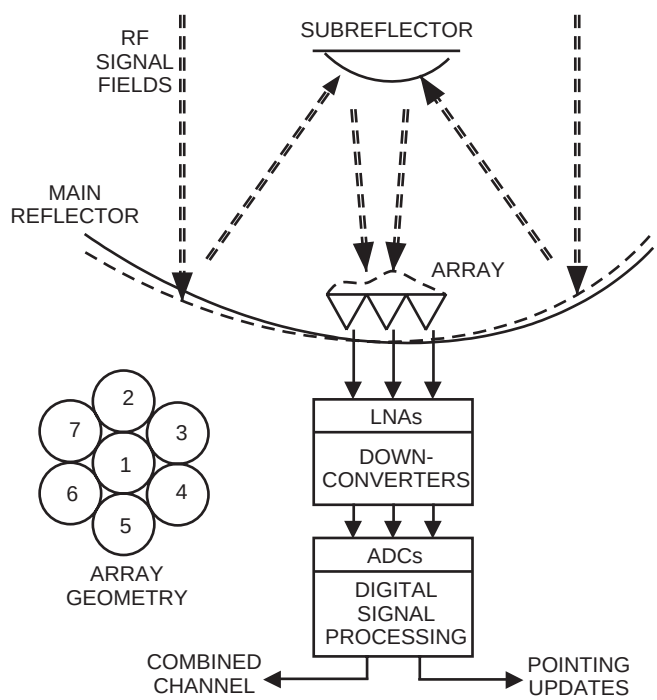

Fig. 1. Conceptual block diagram of the array feed compensation system.

well as an effective defocusing of the power distribution in the focal plane. This defocusing leads to loss of power in the central channel, which nevertheless can be recovered by the outer horns of the array; when multiplied by complex combining weights matched to the instantaneous magnitude and phase of the signal in each channel, the SNR of the combined channel can be improved, approaching that of an undistorted antenna under ideal conditions. Distortions also affect the pointing of the antenna by introducing shifts in the signal peak; our intent here is to demonstrate that properly designed neural-network or least-squares algorithms effectively remove the time-varying pointing offsets and keep the antenna pointed in the desired direction even in the presence of significant antenna distortions and other disturbances.

When the antenna is pointed towards a source such as a distant spacecraft, here assumed to be transmitting a simple unmodulated carrier, the signal in the kth channel can be represented as

$$r_k(t) = s_k(t) + n_k(t), \quad k = 1, 2, \cdots, K \tag{1}$$

where K is the total number of channels (in this case, $K = 7$), and where the signal and background noise components are defined as

$$s_k(t) = \sqrt{2} S_k \cos(\omega t + \theta_k) \tag{2}$$

$$n_k(t) = \sqrt{2}\big[n_{ck}(t)\cos(\omega t) + n_{sk}(t)\sin(\omega t)\big] \tag{3}$$

Here $n_{ck}(t)$ and $n_{sk}(t)$ are uncorrelated baseband random processes representing the in-phase and quadrature-phase components of the noise. Both the amplitude, S_k, and phase, θ_k, of the signal depend on the distortion of the antenna and on the pointing offset. After downconversion to in-phase and quadrature-phase baseband, these waveforms are sampled, yielding the complex samples

$$r_k(i) = s_k(i) + n_k(i), \quad k = 1, 2, \cdots, K \tag{4}$$

with $s_k(i) \equiv S_k e^{j\theta_k}$, $En_k(i) = 0$, and $E|n_k(i)|^2 = \mathrm{var}[r_k(i)] = \sigma^2$, where i refers to the sample number. For simulation purposes, we assume that noise samples from different channels are independent, as are different noise samples in the same channel. It is convenient to represent the received samples as K dimensional vectors, $\mathbf{r}(i) = \mathbf{s}(i) + \mathbf{n}(i)$, where $\mathbf{r}(i) = (r_1(i), r_2(i), \cdots, r_K(i))$ and where each component is defined in Eq. (4). In order to reduce the effect of the noise, one can average a large number of consecutive received vectors,

$$\mathbf{r}_a = \frac{1}{N}\sum_{i=1}^{N} \mathbf{r}(i) \tag{5a}$$

where now

$$\mathrm{var}(r_{a,k}) = \frac{\sigma^2}{N} \tag{5b}$$

and $r_{a,k}$ refers to the kth component of the averaged vector. The averaging of N vectors results in a corresponding reduction in the variance of each averaged sample, as shown in Eq. (5b).

B. Simulation of the Distorted 70-m Antenna

Spacecraft signals received by the seven-channel AFCS were simulated as follows. Physical optics (PO) analysis code was used to obtain the electromagnetic field at the focal plane of the antenna where the apertures of the feed horns are located. This code used the 70-m antenna surface-distortion data obtained from holography measurements during the recent holography-cone experiments [5]. The surface distortions were actually measured at only a few elevation angles, and these data sets were interpolated to obtain distortions at other elevations. The resulting distortions were added to the nominal surface data to obtain the final reflector surface data. The field at the feed horns in the focal plane was obtained by applying a plane wave incident on the main reflector surface and by tracing back to the focal plane via the subreflector.

In the second step, the computed field data were used to obtain the complex voltages at the horn inputs, using a newly developed MATLAB program, as follows. First, the received fields and power in the aperture of each individual horn were calculated. The difference between the power captured by the feed horns and the total power at the focal plane is an indication of feed-array efficiency. In a separate calculation, the fields at the aperture of each horn, induced by the application of a unit voltage to the input of the horn, were calculated by a theoretical waveguide modal expansion. These fields subsequently were convolved with the received focal-plane fields at the aperture of each horn in order to calculate the final complex voltage.

In the application of the antenna distortion model to the current pointing problem, gross antenna elevations of 15, 45, and 75 deg were considered. At each elevation, the voltage response of the horns was simulated for a set of pointing offsets. Each data point consisted of two vectors: a voltage vector of 6 complex numbers, represented as 12 real numbers containing the normalized horn outputs, and a two-dimensional displacement vector containing cross-elevation (XEL) and elevation (EL), in millidegrees.

The voltage vector taken at each data point was normalized by the output of the center horn. This eliminated some time-dependent variations in the signal that may occur in a real-life situation. Since the center horn's normalized output was set equal to $1 + j0$, it was not necessary to present the normalized central horn value to any of the antenna control algorithms. Hence, only six complex numbers needed to be presented to each of the three algorithms under evaluation.

The simulated training data set was generated using a rectangular grid raster scan with antenna displacements ranging from -7 mdeg to $+7$ mdeg in both XEL and EL directions, in 1-mdeg increments. The horn excitations obtained in this manner were noise-free, and this noiseless training set was used to train the RBF network. This training set also was used as a lookup table by the two least-squares algorithms described below.

Test data were generated using independent Gaussian noise samples to simulate various central horn SNR values, with both XEL and EL ranging from -4.67 mdeg to $+4.67$ mdeg in 0.33-mdeg increments. Noise was added prior to normalization since noise in the central horn introduces phase errors in the normalized outer horn voltages when the normalization is performed.

Using the noisy input voltage vectors, the tracking algorithms were used to generate estimates of the true antenna displacement, which then were analyzed to determine acquisition and tracking performance.

C. Description of Acquisition and Tracking Operations

Two distinct problems will be considered in this article: acquisition and tracking. The acquisition problem, which is the focus of much of the current research, involves estimation of antenna-pointing offsets over a wide range. For example, if the antenna's pointing has drifted by 4 mdeg in XEL and -3 mdeg in EL, an acquisition algorithm must be able to estimate the displacement vector $(4, -3)$ accurately and repoint the antenna in the correct direction.

The second problem, tracking, focuses on significantly smaller displacements. After the antenna has been correctly pointed on source by means of the acquisition algorithm, it remains necessary to keep the antenna pointed on source despite possible slow drift in antenna pointing. Accordingly, the tracking algorithm must be able to estimate small pointing errors near the center of the (XEL, EL) space. The distinction between these two problems will be reemphasized later in this article, where both acquisition and tracking problems will be addressed.

II. Algorithm Descriptions

A. Algorithm 1: The Radial Basis Function Network

A radial basis function (RBF) neural network was developed and used to estimate antenna pointing offsets [3,4]. As shown in Fig. 2, this radial basis algorithm takes 13 inputs. The first input is the antenna elevation in radians, used to identify which elevation band of the training data set to use, while the other inputs are the complex baseband outputs of the six outer horns.

As shown in Fig. 2, the RBF network consists of two layers: a nonlinear radial basis function layer and a linear combiner layer. Each radial basis unit implements a Gaussian function of the form $\exp\left(-\left(b\left\|\bar{r}-\bar{c}_i\right\|\right)^2\right)$, where we define $b = 0.8326/\text{spread}$. The vector $\bar{r}$ is the 13-element input vector, and $\bar{c}_i$ is the center of the ith radial basis unit. In other words, $\bar{c}_i$ is the center of the basis unit in the 13-dimensional elevation-voltage space. The squared Euclidean distance between each of these centers and the input vector is calculated for the purposes of determining the output level of each of the radial basis units. The spread is defined such that, when the norm is equal to the spread, $||\bar{r}-\bar{c}_i|| = \text{spread}$, then $\exp\left(-\left(b\left\|\bar{r}-\bar{c}_i\right\|\right)^2\right) = 0.5000$. We can think of spread as defining the localized region of response of the radial basis unit in the complex voltage-elevation input space. The linear combiner simply implements $\overline{a_2} = \overline{W}\overline{a_1} + \overline{b}$, where $\overline{a_1}$ is the vector of radial basis outputs, $\overline{b}$ is a set of bias weights, and $\overline{W}$ is a set of connection weights. The output vector $\overline{a_2}$ is the estimated displacement vector containing both XEL and EL.

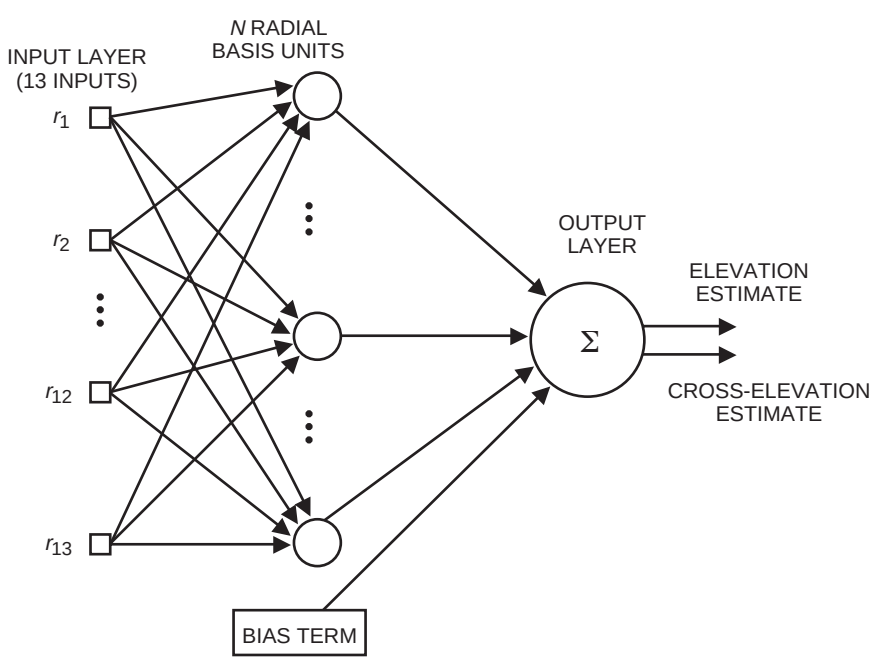

Fig. 2. Radial basis function (RBF) neural network conceptual block diagram.

Therefore, each of the radial basis units receives a 13-element input vector and computes the squared Euclidean distance from the input vector to its 13-dimensional center vector. The output of the radial basis unit is a number that depends on this squared distance. It is equal to unity when the input vector coincides perfectly with the center of the basis unit; if the input vector does not coincide with the basis unit center, then the basis unit's output will be a positive number less than unity, decreasing to zero in the limit as the squared Euclidean distance between the basis unit center and the input vector goes to infinity. There could be any number of basis units, which also are referred to as hidden layer units, in an RBF network. This number varies depending on the complexity of the function being approximated and may be quite large in certain cases.

B. Algorithm 1: RBF Network Training

The RBF network was designed using the computationally efficient orthogonal least-squares algorithm described in [3]. This algorithm uses the training data points as radial basis function centers, where Gaussian radial basis functions are employed in the single hidden (radial basis) layer and a linear combiner with bias weights is used in the output layer. The optimum weights were obtained as the solution to the least-squares fitting problem, as outlined in [3,4].

Since the complex voltage of the center horn always was normalized to $1 + j0$, it was not necessary to provide this input to the network. This normalization effectively eliminates some possible time-dependent variations in the received signal, at the cost of a slight reduction in the total information presented to the algorithms. The network's inputs, therefore, consisted of the antenna elevation in radians and the real and imaginary components of the six normalized horn voltages from the outer horns, for an input vector dimension of 13. The network was trained to generate values for the incremental EL and XEL offsets corresponding to the inputs.

Differences in the antenna's distortion at different gross elevations led to the training of three separate RBF networks for gross elevations of 15, 45, and 75 deg. The experimentally derived basis widths and the number of basis units required are shown in Table 1. The selection of the radial basis function widths was guided by the distances between the input vectors in the training set and by experimentation. Note the use of a much larger spread at 75 deg due to severe antenna distortion at high elevation.

Table 1. The number of hidden layer radial basis units and the corresponding radial basis spreads of the RBF network.

Gross elevation, deg	Radial basis spread, mdeg	Number of radial basis units N
15	0.50	127
45	0.70	103
75	2.50	77

C. Algorithm 2: Quadratic Interpolated Least Squares

The non-interpolated least-squares algorithm compares the six complex outer horn voltages with a set of reference vectors in the training data set. The reference vector closest to the observed vector (in the Euclidean sense) is taken to be the true vector, and the antenna displacement corresponding to that vector is returned as the algorithm's estimate of the instantaneous pointing offset. However, since very fine quantization of the training data set requires a great deal of storage along with time-

consuming computations, some form of interpolation of coarse-quantized training data would be useful for synthesizing finer antenna displacements in XEL and EL.

The following interpolation scheme was devised: define "voltage space" to be the vector space consisting of the vectors of complex horn voltages for the 6 outer horns. Each of these horns has a complex baseband output, and the resulting vector of normalized outer-horn voltages contains 6 complex numbers, or equivalently 12 real numbers. The space of these vectors comprises the voltage space. We also consider the two-dimensional space of vectors describing displacements in XEL and EL. These vectors represent the physical antenna-pointing offsets, and the correspondence between the vectors in voltage space and the displacement vectors in antenna-offset space is used for interpolation by both the interpolated least-squares algorithm and the RBF network.

In the interpolated least squares algorithm, let d denote the Euclidean distance from the input voltage vector to a reference data set vector. We can approximate "d" using the following equation in antenna offset space:

$$d = \sqrt{\left(a_1^2 \left(XEL_{\text{true}} - XEL_{est}\right)^2 + a_2^2 \left(EL_{\text{true}} - EL_{est}\right)^2\right)} \tag{6}$$

This is seen to be a quadratic approximation to the error surface near the true displacement. Using optimization techniques to simultaneously solve for a_1, a_2, XEL_{true}, and EL_{true}, we can estimate XEL_{true} and EL_{true} from the values of d and from the quantized values of XEL and EL in the training data set.

Nine estimated values of XEL and EL were obtained as follows: as with the standard least-squares algorithm without interpolation, we begin by selecting the voltage vector closest to the input vector. We then take the displacement vector from the training data corresponding to this voltage vector. This is the initial estimate of displacement to provide us with initial values of XEL_{est} and EL_{est}. Next, focusing on the displacement space, we select the eight displacement vectors closest to our initial choice from the training data. Since the training data were formed using a 1-mdeg rectangular grid scan, we now have a box with 2-mdeg sides containing nine points. The Euclidean distance d in voltage space is calculated for each of the nine points, and the above expression is solved using optimization techniques to find the closest fit for XEL_{true} and EL_{true}. This is the interpolated estimate of the antenna-pointing offset for a given voltage vector.

D. Algorithm 3: Fuzzy Interpolated Least Squares

A simpler interpolation strategy, which does not require any assumptions about the shape of the error surface, is a "fuzzy" interpolation strategy. This is based on the idea of exponential fuzzy membership functions found in fuzzy set theory. Let d be the Euclidean distance between the input voltage vector and a voltage vector from the training data set, and calculate the weight term $w = e^{-d}$. The idea is to take the same nine points as with the quadratic interpolated least-squares algorithm and weight each of them with a number calculated from the distance in voltage space. Therefore, if we let $\{\,\overline{v_1} \quad \overline{v_2} \quad \overline{v_3} \quad \overline{v_4} \quad \overline{v_5} \quad \overline{v_6} \quad \overline{v_7} \quad \overline{v_8} \quad \overline{v_9}\,\}$ denote the set of nine displacement vectors, we can compute an estimate of the antenna's displacement by taking a weighted sum of the form

$$\frac{\sum_{i=1}^{9} w_i \overline{v_i}}{\sum_{i=1}^{9} w_i}$$

The weights in this sum are determined using fuzzy membership functions; hence, an estimate obtained in this manner could be called a "fuzzy estimate" of the antenna's displacement.

III. Performance Comparisons

A. Acquisition Mode

Figures 3 through 12 illustrate the mean error and error standard deviation (or rms error) of the RBF network and the two interpolated least-squares algorithms defined previously. In the following figures, both the mean errors and the standard deviations have been averaged over the entire acquisition range. It should be noted that, for RBF networks with 10-s averaging, mean errors generally are less than 0.1 mdeg for SNRs above 15 dB-Hz, as illustrated by Fig. 3(a) for 45-deg elevation and Fig. 3(b) for 75-deg elevation. These figures also show much larger mean errors if only 1-s integration is used. It is interesting that at low SNRs smaller mean errors were obtained at 75 deg than at 45 deg, even though the antenna is least distorted at 45 deg (corresponding to the rigging angle, where the panels were originally set to generate the desired shape). This may be due to the fact that, at higher elevations, more signal power is projected onto the outer horns due to the greater antenna distortion, possibly providing better pointing information as the distorted patterns are scanned off source. Figures 4(a) and 4(b) illustrate noticeable mean errors of approximately 0.2 mdeg associated with the quadratic least-squares algorithm even at high SNRs. The improved mean-error performance of the fuzzy least-squares algorithm in this region is shown in Figs. 5(a) and 5(b), where mean errors are seen to be approaching zero with increasing SNR, as expected.

At low SNRs, error standard deviations were generally much larger than mean errors and, therefore, in this region the rms errors constitute the main error component. Figures 6(a) and 6(b) illustrate the improved performance of 10-s integration over 1-s measurements. Note that 10-s integration has a significant advantage over 1-s integration, generally achieving the expected factor of 3 decrease in standard deviation (or factor of 10 decrease in estimation variance) over 1-s data.

Figures 7(a) through 8(b) illustrate the error standard deviation of the quadratic and fuzzy interpolated least-squares algorithms. It is interesting that at high SNRs neither algorithm continues to improve with increasing SNR as expected, but tends to approach an rms error floor of a few tenths of a millidegree. This irreducible error appears to be due to decreased accuracy of the interpolation algorithms near the outer edges of the acquisition range, where simple approximations to the error surface tend to break down.

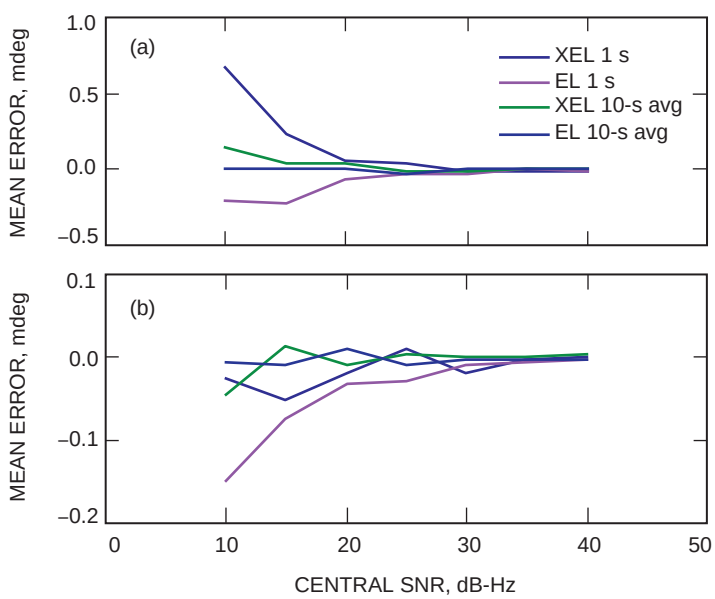

Fig. 3. Average offset for the RBF neural network versus SNR at elevations of (a) 45 deg and (b) 75 deg.

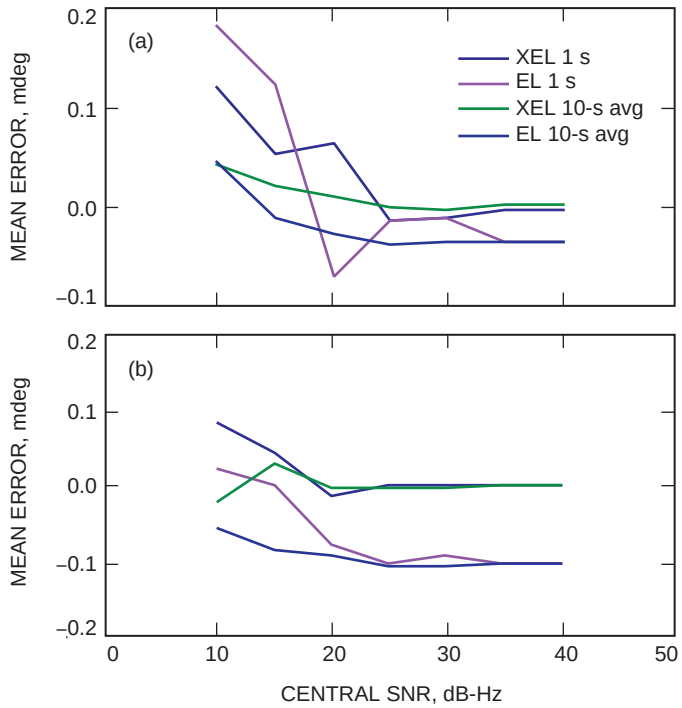

Fig. 4. Average offset for quadratic least squares versus SNR at elevations of (a) 75 deg and (b) 45 deg.

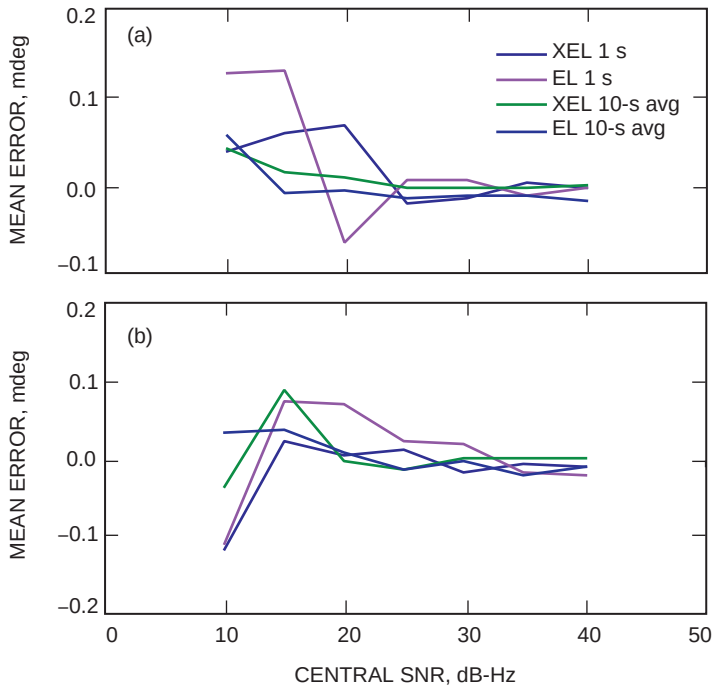

Fig. 5. Average offset for fuzzy least squares versus SNR at elevations of (a) 45 deg and (b) 75 deg.

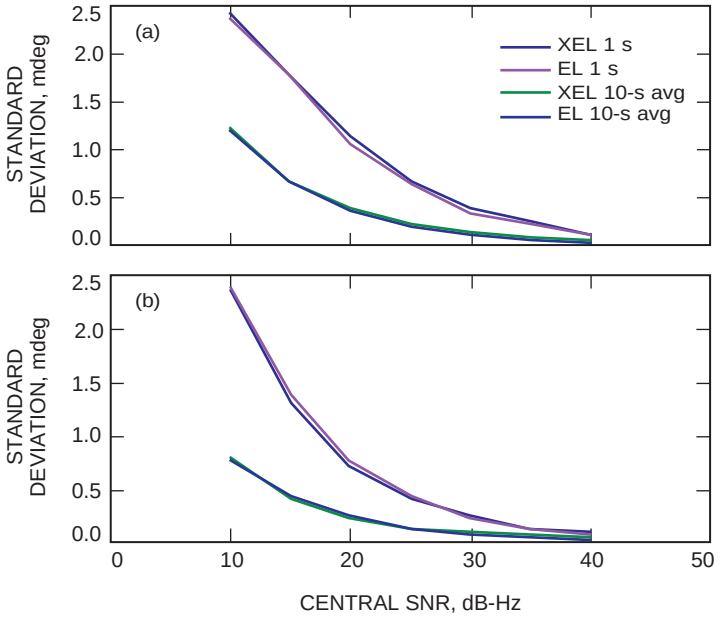

Fig. 6. RBF neural network rms error versus SNR at elevations of (a) 45 deg and (b) 75 deg.

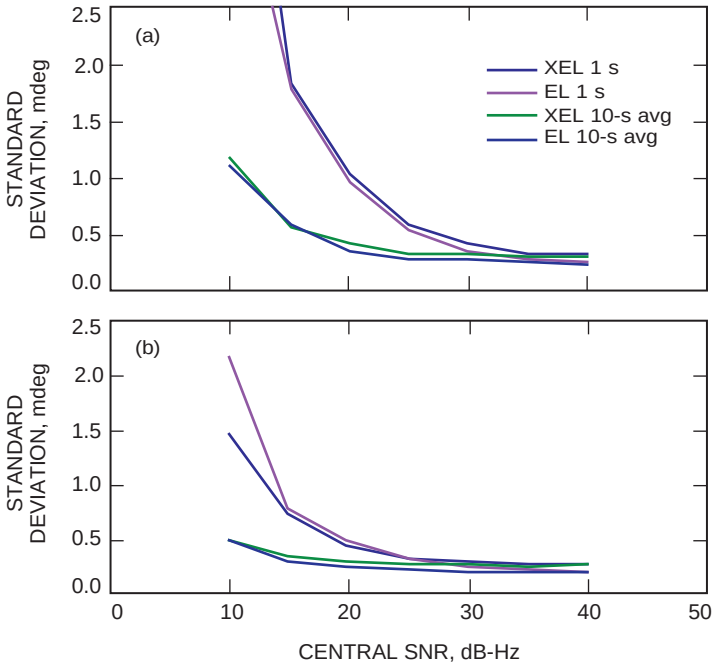

Fig. 7. Quadratic least-squares rms error versus SNR at elevations of (a) 45 deg and (b) 75 deg.

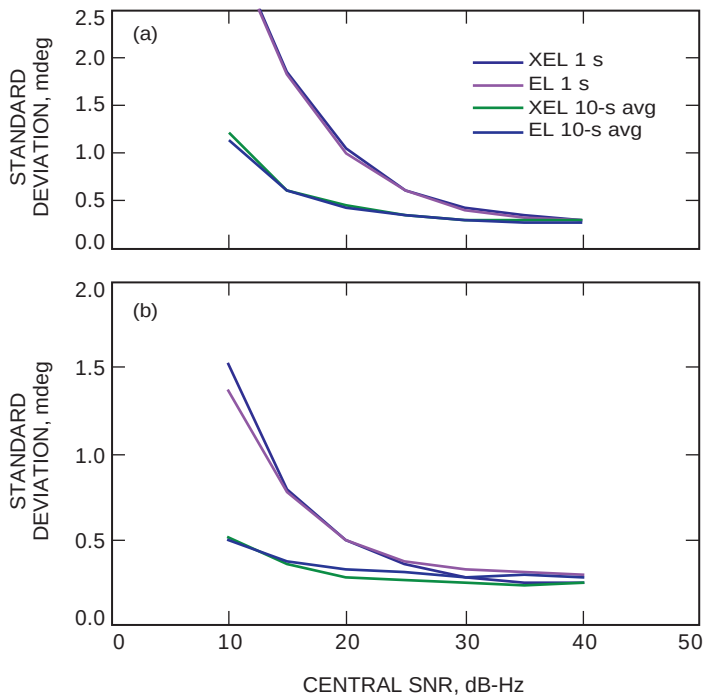

Fig. 8. Fuzzy least-squares rms error versus SNR at elevations of (a) 45 deg and (b) 75 deg.

Figures 9 through 12 compare the error standard deviations of all three algorithms when operating in acquisition mode, at varying SNR levels, and using 10-s averaging. It can be seen that, for medium to high SNRs (greater than 20 dB-Hz), the RBF network outperforms the least-squares algorithms in acquisition mode, whereas, in the low SNR region from 10 dB-Hz to approximately 20 dB-Hz, the least-squares algorithms yield best performance. These results suggest the use of a hybrid system consisting of a least-squares algorithm for low-SNR acquisition and a radial basis function network for the medium- to high-SNR regions.

In summary, these simulations have demonstrated that the RBF neural network yields the best mean-error and rms-error performance in the medium- to high-SNR range (i.e., for SNRs in excess of 20 dB-Hz) during acquisition. However, under very noisy conditions in acquisition mode, the least-squares algorithms yield the lowest rms and mean errors; hence, these algorithms are preferred in the low-SNR regions.

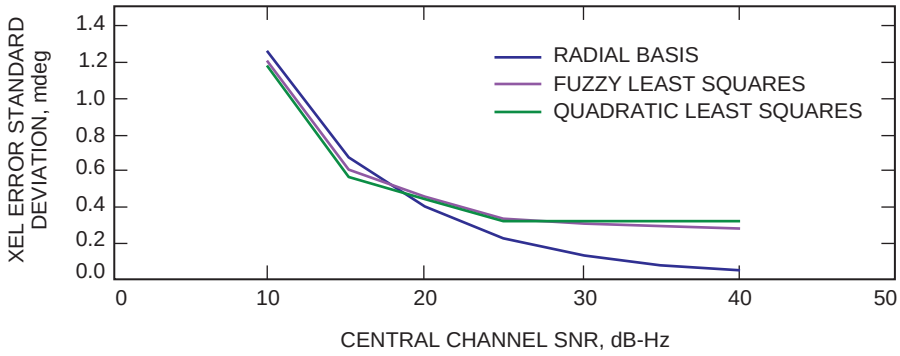

Fig. 9. Comparison of rms XEL error versus SNR in acquisition mode, 45-deg elevation.

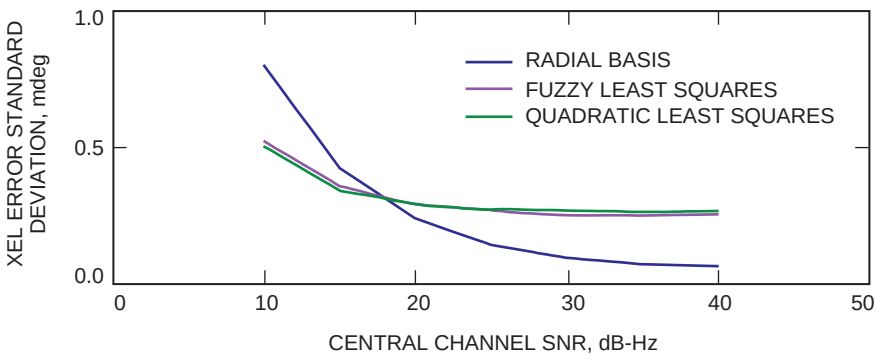

Fig. 10. Comparison of rms XEL error versus SNR in acquisition mode, 75-deg elevation.

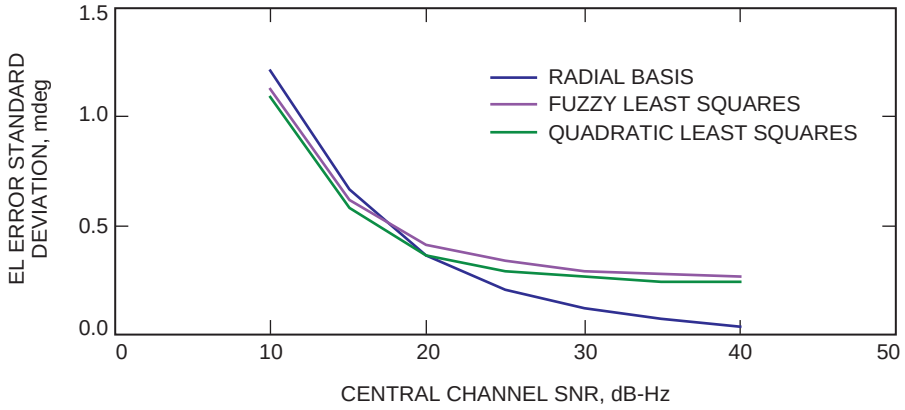

Fig. 11. Comparison of rms EL error versus SNR in acquisition mode, 45-deg elevation.

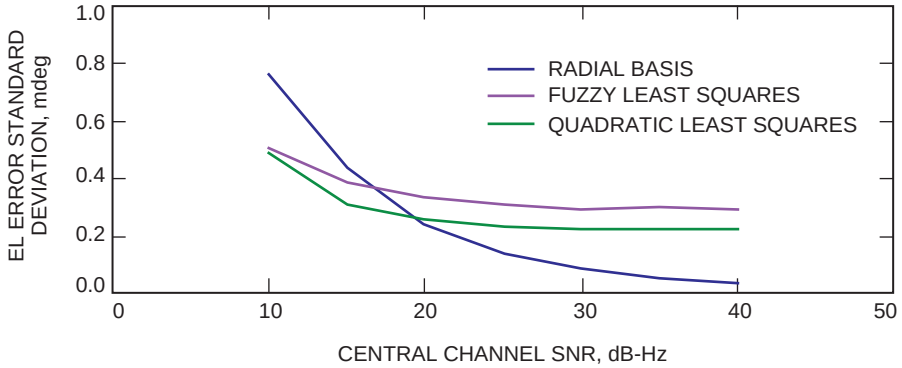

Fig. 12. Comparison of rms EL error versus SNR in acquisition mode, 75-deg elevation.

B. Tracking Mode

The results shown above demonstrate the overall accuracy of these algorithms taken over a large test grid of points from −5 mdeg to +5 mdeg in both the XEL and EL directions, which has been designated as the acquisition mode. Accuracy near the center of the test grid, commonly referred to as tracking, is also of interest, particularly when tracking a source under nominal conditions, so that large unexpected pointing offsets are not likely. Since the RBF neural network was not trained over this narrower tracking range, its performance in tracking mode will not be presented here; however, since the structure of the quadratic least-squares algorithm need not be modified for it to be effective in tracking as well as acquisition applications, its performance in tracking mode can be meaningfully evaluated.

Scatter diagrams were generated for two distinct cases in tracking mode: the true on-source case corresponding to (0,0) mdeg in the (XEL, EL) plane and a slightly off-source case at coordinates (0, 1/3) mdeg, both at 75-deg elevation. The performance of the quadratic least-squares algorithm for these two cases at a high SNR (40 dB-Hz) is illustrated in Figs. 13 and 14. Note that all of the points plotted correspond to 1-s integrations.

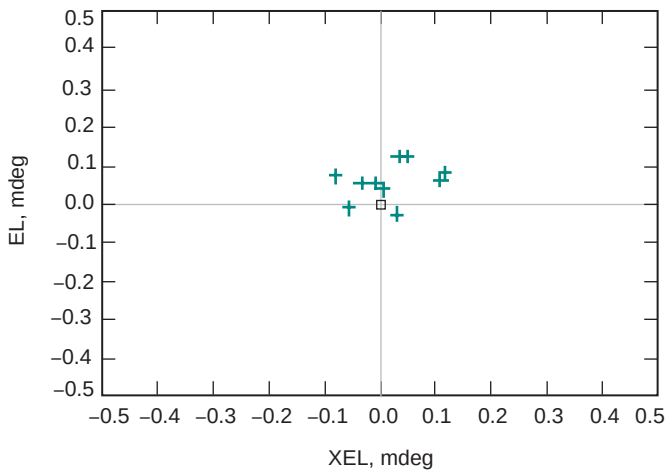

Fig. 13. Scatter diagram for quadratic least-squares algorithm in tracking mode, on-source case.

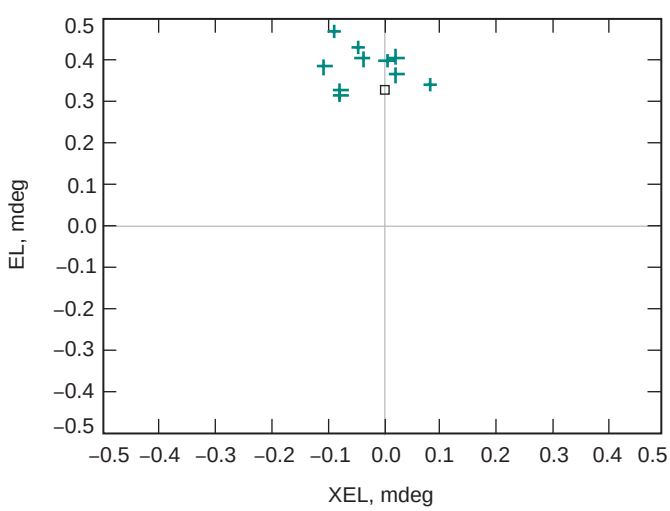

Fig. 14. Scatter diagram for quadratic least-squares algorithm in tracking mode, 0.33-mdeg off-source case in the EL direction.

The rms errors of the quadratic least-squares algorithm near the center of the (XEL, EL) plane (the nominal on-source direction) are shown in Table 2. Note that there is no noticeable tracking offset and that rms errors are extremely small in both directions for this high-SNR case, on the order of 0.05 to 0.07 mdeg, which is completely negligible for practical tracking applications.

The performance of the least-squares algorithm with quadratic interpolation is shown in Figs. 15 through 17 at three different elevations over a range of SNR values. Again, 1-s integration was employed.

Table 2. Quadratic rms errors corresponding to Figs. 13 and 14.

Center		(0,1/3)	
XEL, mdeg	EL, mdeg	XEL, mdeg	EL, mdeg
0.06521	0.048721	0.060459	0.047572

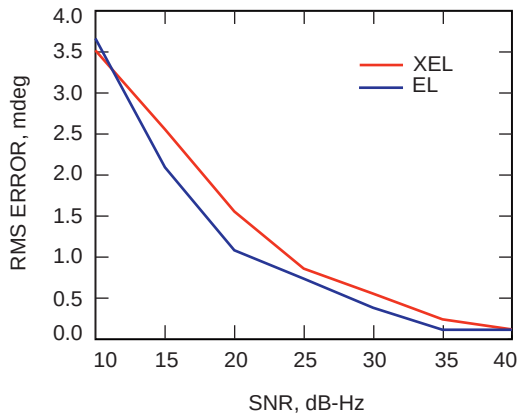

Fig. 15. Tracking performance of the quadratic least-squares algorithm, 15-deg elevation.

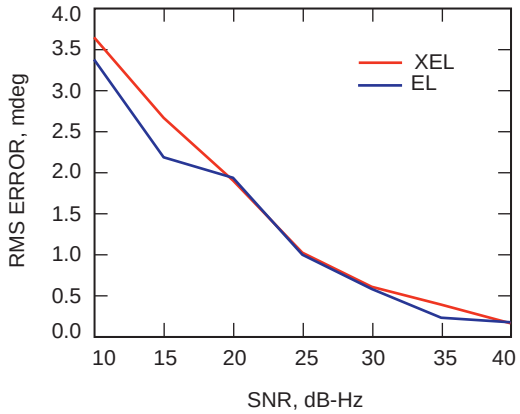

Fig. 16. Tracking performance of the quadratic least-squares algorithm, 45-deg elevation.

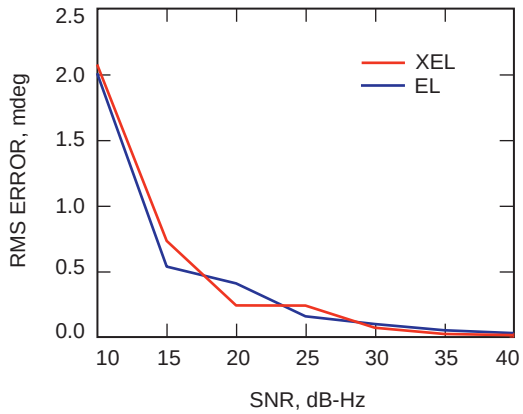

Fig. 17. Tracking performance of the quadratic least-squares algorithm, 75-deg elevation.

Note that, for all elevations considered, rms errors remain lower than 1 mdeg in both directions for all SNRs greater than about 25 dB-Hz, which can be further reduced with longer integration times. While in tracking mode, the error-floor effect noted in acquisition mode (that is, evaluated and averaged over a much larger operating range) does not occur, confirming that the quadratic approximation is accurate near the center of the test grid; in tracking mode, the pointing estimates of the least-squares algorithm continue to improve with increasing SNRs, as expected.

These results indicate that above 35 dB-Hz and with 1-s integration this algorithm tracks with rms error of less than 0.5 mdeg even in the presence of severe distortion, demonstrating the ability of the AFCS to point the 70-m antenna with an accuracy exceeding current DSN requirements under nominal operating conditions.

In order to verify the proper operation of the two-dimensional quadratic approximation algorithm, a simpler algorithm consisting of two one-dimensional quadratic cuts through the two-dimensional surface also was implemented. Performance of this simpler algorithm should approach that of the two-dimensional algorithm under ideal conditions (that is, when the surface is rotationally symmetric and undistorted), but in general it provides a useful upper bound on performance. Comparisons of this simple bound with the true optimal quadratic interpolation algorithm are shown in Figs. 18 and 19 as a function of SNR (1-s integration) at elevations of 15 and 75 deg. These simulations indicate that two-dimensional interpolation indeed achieves a slight improvement; however, because of its simplicity and greater speed, the simple bounding algorithm may provide an easily implementable alternative to the two-dimensional formula.

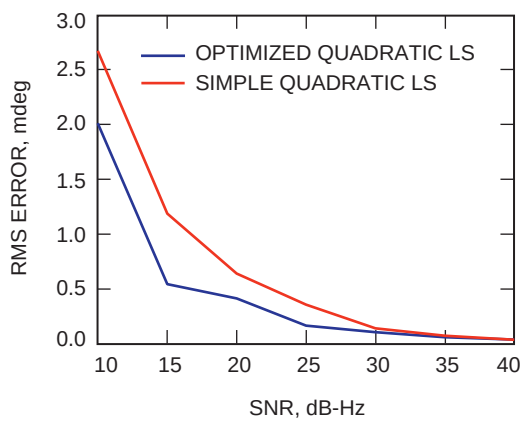

Fig. 18. Comparison of the optimal and simple quadratic least-squares (LS) interpolation algorithms, 75-deg elevation.

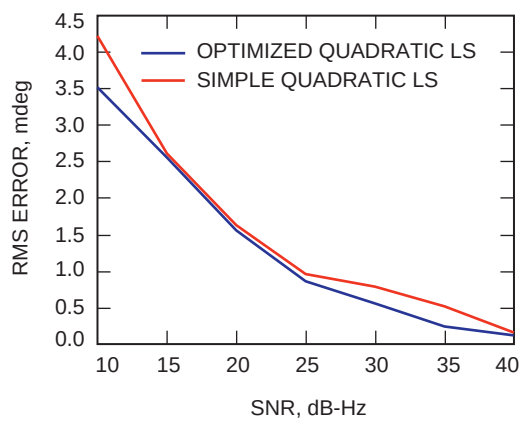

Fig. 19. Comparison of the optimal and simple quadratic interpolation algorithms, 15-deg elevation.

IV. Summary and Conclusions

The gravity-distorted antenna profile, based on holography cone measurements of the 70-m antenna at Deep Space Station 14 (DSS 14) [5], was simulated at elevations of 15, 45, and 75 deg. This simulation was used to evaluate two different acquisition algorithms: an RBF neural network and a least-squares algorithm employing either quadratic or fuzzy logic interpolation. Performance of the quadratic least-squares algorithm was evaluated in both acquisition and tracking modes, but the RBF neural network was evaluated only in acquisition mode, for which it was trained. It was found that, in acquisition mode with medium to high central horn SNRs (20 dB-Hz or greater), the RBF network yielded the best overall pointing-error estimates. Error standard deviations for the RBF network generally were less than 0.5 mdeg for SNRs exceeding 30 dB-Hz and approximately 0.2 mdeg for the high-SNR region near 40 dB-Hz with 1-s integration; with 10-s integration, these errors were further reduced to approximately 0.1 mdeg at

high SNRs. In tracking mode, the quadratic least-squares algorithm achieved rms tracking errors of less than 0.1 mdeg at high SNRs. Furthermore, in the low-SNR region corresponding to 15 dB-Hz or less, the least-squares algorithm appears to yield the best acquisition and tracking performance, with negligible mean offsets and generally lower rms errors than those achieved by the RBF neural network.

However, we need to emphasize that real-world effects, such as wind and possible antenna vibrations, commonly encountered during actual tracking were not included in the simulation models. The performance of these algorithms in the field may be degraded by these unmodeled disturbances; hence, the extremely small pointing errors predicted at high SNRs may not be achievable in practice. It is, therefore, important to complete the algorithm development by experimentally demonstrating the true acquisition and tracking performance of these algorithms on a 70-m antenna.

Directions for future research include the addition of new capability to enable adaptation of the RBF network's linear combining weights to slow changes in the antenna deformation caused by aging or seismic activity. The design of algorithms that respond to rapid changes in the deformation parameters of the antenna caused by wind gusts and accurate real-time measurement of these changes to enable control of mechanical compensating surfaces for best overall performance remain to be investigated.

Acknowledgment

The authors wish to express their gratitude to Dave Fort for many important insights and suggestions during the course of this research.

References

[1] V. A. Vilnrotter, E. R. Rodemich, and S. J. Dolinar, Jr., "Real-time Combining of Residual Carrier Array Signals Using ML Weight Estimates," *IEEE Trans. Communications*, vol. 40, pp. 604–615, March 1992.

[2] A. R. Cherrete, R. J. Acosta, P. T. Lam, and S. W. Lee, "Compensation of Reflector Antenna Surface Distortion Using an Array Feed," *IEEE Trans. Antennas and Propagation*, vol. 37, pp. 966–978, August 1989.

[3] S. Chen, C. F. N. Cowan, and P. M. Grant, "Orthogonal Least Squares Learning Algorithm for Radial Basis Function Networks," *IEEE Trans. Neural Networks*, vol. 2 no. 2, pp. 302–309, March 1991.

[4] S. Haykin, *Neural Networks: A Comprehensive Foundation*, New York: Macmillan, pp. 256–268, 1994.

[5] V. Vilnrotter and D. Fort, "Demonstration and Evaluation of the Ka-Band Array Feed Compensation System on the 70-Meter Antenna at DSS 14," *The Telecommunications and Mission Operations Progress Report 42-139, July–September 1999*, Jet Propulsion Laboratory, Pasadena, California, pp. 1–17, November 15, 1999.
http://tmo.jpl.nasa.gov/tmo/progress_report/42-139/139J.pdf